

# Electrically tunable flat bands with layer-resolved charge distribution in twisted monolayer-bilayer graphene

Wei-En Tseng<sup>1,2</sup> and Mei-Yin Chou<sup>1,2</sup>

<sup>1</sup>*Institute of Atomic and Molecular Sciences, Academia Sinica, Taipei 10617, Taiwan*

<sup>2</sup>*Department of Physics, National Taiwan University, Taipei 10617, Taiwan*

At a small twist angle, exotic electronic properties emerge in twisted monolayer-bilayer graphene (aAB), including electrically switchable magnetic order and correlated insulating states. These fascinating many-body phenomena manifest when the low-energy bands feature a narrow band width. In this study, we examine the electronic structure of aAB using first-principles calculations combined with an accurate tight-binding model. We find that the presence of an intrinsic polarization greatly modifies the low-energy bands of aAB. Furthermore, the low-energy bands reach a minimum width at a quasi-magic angle and feature a layer-dependent charge localization and delocalization pattern. In the presence of an electric field, an energy gap opens only if lattice relaxation is taken into account. The particle-hole asymmetry in aAB further leads to flatter conduction bands compared with the valence bands, with an electrically tunable band width and band gap, and a switchable sublattice-dependent charge localization and delocalization pattern.

## I. INTRODUCTION

The unexpected special electronic properties in magic-angle twisted bilayer graphene (TBG) have given rise to features such as correlated insulating phases [1, 2], superconductivity [2, 3], orbital ferromagnetism [2, 4], and Chern insulators [5–7]. Recently, investigations of twistronics have expanded to twisted trilayer graphene with different geometric stacking patterns. For example, a robust superconducting phase with electric-field tunability [8–11] has been observed in alternating twisted trilayer graphene (TTG) near its magic angle. Due to the presence of mirror symmetry in TTG, its Hamiltonian can be decomposed into an effective TBG part plus a decoupled monolayer by a proper transformation [12, 13]. In contrast, twisted monolayer-bilayer graphene has a lower crystal symmetry (absence of inversion and mirror symmetry), and no simple mathematical connection is found between its Hamiltonian and that of TBG. Depending on the direction of an external electric field, it may exhibit a similar phase diagram as TBG or twisted double bilayer graphene (TDBG) [14]. In the following, we denote twisted monolayer-bilayer graphene as aAB, where “a” represents the twisted monolayer on top of the underlying untwisted “AB” Bernal bilayer.

Remarkably, aAB demonstrates a strong electrical tunability of its correlated states [14–20] and van Hove singularities [15]. Specifically, when an external electric field is applied from the monolayer side to the bilayer, correlated insulating states were observed at integer fillings of the conduction bands [16, 17]. In addition, quantum anomalous Hall effect in an orbital Chern insulator is realized due to the interplay between electron correlation and non-trivial band topology [17, 18]. In particular, at a filling of three electrons per moiré unit cell, the Chern number and associated magnetic order can be switched by the electric field [17, 18], making aAB possible to realize non-volatile switching of magnetization. Furthermore, a Chern insulator was even observed at fractional

fillings, with topological charge density waves breaking the translational symmetry of the moiré [19]. The emergence of correlated insulating states may be attributed to spontaneous flavor symmetry breaking [17–20] or the formation of an electron crystal [16]. On the other hand, when the electric field is applied in the opposite direction (from the bilayer to the monolayer), the correlated states in the conduction bands exhibit a metallic behavior [14, 20], and an electrically switchable anomalous Hall effect was observed [14], indicating the presence of abundant orbital magnetism in the aAB system.

The rich phase diagram of aAB observed in a range of twist angles from  $1.0^\circ$  to  $1.4^\circ$  is believed to arise from the flat bands, where the electron’s kinetic energy is greatly reduced. Therefore, it is crucial to understand theoretically the nature of flat bands and its interplay with the external electric field. While previous numerical calculations based on a continuum model have revealed the presence of topological flat bands with electrically tunable Chern numbers [21–23], the characteristics of the flat bands differ in models due to different empirical parameters used. In addition, it was pointed out that the second nearest-neighbor interlayer hopping terms between the Bernal bilayer, which correspond to trigonal warping and electron-hole asymmetry, have a significant impact on the band structure [21, 22]. However, these coupling terms are still short-range interactions, and a detailed analysis of the electronic structure considering more accurate long-range interactions is still lacking to date.

In this work, we perform first-principles calculations and a tight-binding model with accurate angle-dependent interlayer couplings [24, 25] to study the electronic properties of aAB. Our results show that the presence of an intrinsic polarization splits the parabolic bands of aAB. In addition, the low-energy bands possess a minimum width at an angle that correlates with the first magic angle of TBG. We further identify this angle in aAB as the quasi-magic angle. Near the quasi-magic angle, we find charge localization in the adjacent twisted layers and de-

localization in the outer Bernal layer. Subsequently, we explore the impact of an electric field on the band structure. Our findings demonstrate that the field-induced energy gap only opens when the effect of atomic relaxation is included. The band widths of the resulting conduction and valence bands can further be tuned by an electric field, with the conduction bands generally flatter. In addition, the applied electric field leads to charge redistribution in the flat bands, resulting in a unique sublattice-dependent charge localization and delocalization pattern within a single layer.

## II. RESULTS AND DISCUSSIONS

### A. Atomic configurations of twisted monolayer-bilayer graphene

In this work, we consider commensurate aAB structures with the moiré lattice vectors defined as  $\mathbf{L}_1 = m\mathbf{a}_1 + (m+1)\mathbf{a}_2$  and  $\mathbf{L}_2 = -(m+1)\mathbf{a}_1 + (2m+1)\mathbf{a}_2$ , where  $m$  is an integer, and  $\mathbf{a}_1$  and  $\mathbf{a}_2$  represent the lattice vectors for monolayer graphene. Figure 1 illustrates the moiré pattern of aAB with a twist angle  $\theta = 2.64^\circ$  ( $m = 12$ ). The local atomic configurations vary within the moiré supercell, and the three high-symmetry stacking patterns are labeled as AAB, BAB, and CAB.

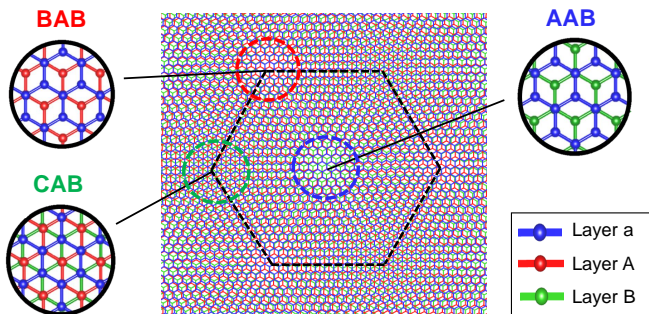


FIG. 1. Moiré pattern of aAB with a twist angle  $\theta = 2.64^\circ$ . The top layer (labeled as layer “a”) is rotated with respect to the AB-stacked bilayer graphene. In our convention, layer A and layer B refer to the middle and bottom layers, respectively. The black dashed hexagon represents the Wigner-Seitz moiré supercell, with the three high-symmetry stacking patterns labeled as AAB, BAB, and CAB.

### B. Electronic structure with intrinsic polarization

Figure 2(a)-(b) show layer-projected band structures for  $\theta = 13.2^\circ$  and  $\theta = 5.1^\circ$  from density functional theory (DFT) calculations. In the low-energy regime, aAB features four bands composed of the Dirac bands doubly degenerate at K originating from the twisted monolayer and two parabolic bands originating from the AB-bilayer.

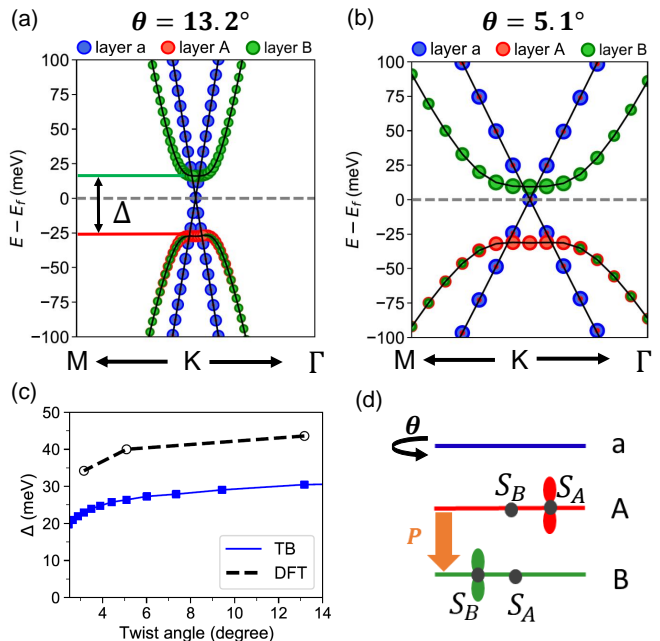


FIG. 2. Layer-projected band structure of aAB at twist angles (a)  $\theta = 13.2^\circ$  and (b)  $\theta = 5.1^\circ$  calculated by DFT. At these large twist angles, the Dirac bands are mainly contributed from layer a, and the parabolic bands originating from the AB-bilayer have a significant splitting  $\Delta$  of about 40 meV induced by an intrinsic polarization. The lengths of  $\overrightarrow{MK}$  and  $\overrightarrow{K\Gamma}$  directions are taken as half of the distance from M to K point. (c) Comparison of the splitting  $\Delta$  calculated from DFT and the TB model as a function of the twist angle. (d) Intrinsic polarization in aAB caused by layer-asymmetric charge transfer. The red and green  $p_z$  orbitals show the layer and sublattice-dependent charge distribution of the parabolic VBM and CBM states, respectively.

At these large twist angles, our calculations uncover a significant splitting  $\Delta$  of the parabolic bands of nearly 40 meV, which was not found in the previous continuum model or tight-binding calculations [26]. The split parabolic VBM and CBM states mainly distribute on layer A and B, respectively, and the degenerate Dirac states reside inside the gap between them. Away from the band edge, the parabolic bands have contributions from layer A and B equally [equal sizes of the layer-projected circles in Fig. 2(a)-(b)].

While the splitting of the parabolic bands can be understood by its interaction with the monolayer Dirac cone, one does not expect a significant splitting to occur at a large twist angle in the absence of an external electric field from the perspective of a continuum model. This is because the large separation between the Dirac cone and the parabolic bands in the momentum space results in a weak interaction between them. We explain this splitting of parabolic bands by the presence of an intrinsic polarization in the vertical direction. This intrinsic polarization is induced by an asymmetric charge transfer across the layers, since both the inver-

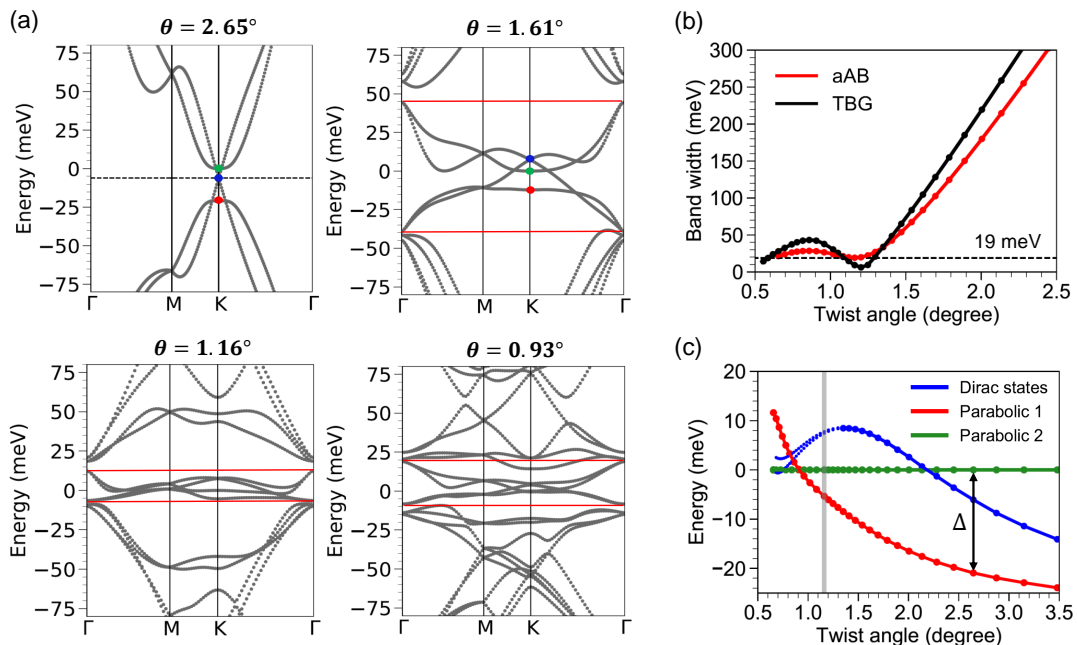


FIG. 3. (a) Band structures of aAB at small twist angles, with the band width of the low-energy bands marked by red lines. The blue, red, and green dots label the Dirac states, parabolic state 1 (parabolic VBM) and parabolic state 2 (parabolic CBM). (b) Band width as a function of twist angle for aAB and TBG. At  $\theta = 1.16^\circ$ , the low-energy bands of aAB reach a minimum band width of about 19 meV (marked in a horizontal dashed line). Here, we define this special angle as the quasi-magic angle (qMA). (c) The eigenvalues of the four states at the K point as a function of twist angle. The parabolic state 2 has a pinned eigenvalue, and thus is set to zero energy. The splitting between the parabolic states is labeled as  $\Delta$ . The degenerate Dirac states split in energy at small angles, as represented by small blue dots. The vertical grey line marks the qMA ( $\theta = 1.16^\circ$ ).

sion symmetry and mirror symmetry are broken in aAB. It can be seen from the layer-projected band structure that the occupied parabolic VBM is mainly composed of layer A, while the unoccupied parabolic CBM has a main contribution from layer B, resulting in a charge transfer from layer B to A. Therefore, the intrinsic polarization of aAB points from layer A to layer B, as shown in Fig. 2(d). The red and green  $p_z$  orbitals demonstrate the layer and sublattice-dependent charge distributions of the parabolic VBM and CBM states, respectively. This visualization is valid only for a large twist angle when the layer hybridization is not strong. The vertical dipole moment of aAB can be calculated by the Berry phase method [27] using DFT. For a large twist angle  $\theta = 13.2^\circ$ , we estimate the dipole moment to be  $0.019 e \cdot \text{\AA}$  in one supercell, which corresponds to an electrical polarization of 0.3 pC/m.

Here, we compare the splitting  $\Delta$  from our tight-binding (TB) and DFT calculations at different twist angles, and find that they are in good consistency as shown in Fig. 2(c). The splitting of parabolic bands gradually decreases as the twist angle decreases. In TB calculations, we find that the main reason for this significant splitting is an accurate description of the angle-dependent interlayer coupling between a and A layers, which is needed in studying the low-energy bands of aAB. Using simplified TB parameters may not be able to capture this feature correctly. The splitting of parabolic

bands in aAB we have observed is reminiscent of that in twisted double-bilayer graphene (TDBG), where a gap separates the conduction and valence parabolic bands with charge located in the outer layers and the inner layers, respectively [28, 29]. This phenomenon observed in TDBG was attributed to the internal crystal fields pointing from the surfaces towards the inner layers [28, 30]. In contrast to aAB, however, the internal crystal fields in TDBG nearly cancel out and do not generate a net electric polarization due to layer symmetry.

### C. Flat bands and quasi-magic angle

The band structures of aAB at small twist angles are calculated using the tight-binding model as shown in Fig. 3(a). As the twist angle decreases, the features of the four low-energy bands (parabolic bands and Dirac bands) can still be identified, although distortion occurs. The four bands at low energies are separated from the rest, and the energy order of the linear Dirac bands and parabolic bands are also varied. Therefore, a more reasonable parameter to be considered is the whole band width. Figure 3(b) shows that the band width of the four low-energy bands in aAB does not decrease monotonically with the twist angle. Instead, its variation as a function of the twist angle demonstrates a high similarity with that in TBG. We find that the low-energy bands of

aAB reach a minimum band width of approximately 19 meV at a twist angle of about  $1.16^\circ$ , which is close to the first magic angle of TBG. Here, we define this special twist angle in aAB as the quasi-magic angle (qMA), since the four low-energy bands of aAB at  $1.16^\circ$  are not as flat as those in TBG or TTBG at the magic angles. In the vicinity of the qMA, the band width of aAB is slightly larger than that of TBG, but this situation reverses when the twist angle deviates about  $0.1^\circ$  away from this value. We also discuss the variation of the qMA in aAB under an external pressure in Supplementary Materials.

Next, we analyze the energy variations of the four states at the K point when the twist angle decreases as shown Fig. 3(d). In the case of small twist angles, we name the parabolic VBM state as parabolic state 1 and the parabolic CBM state as parabolic state 2. The positions of the Dirac point, parabolic state 1 and parabolic state 2 in the band structure (Fig. 3(a)(b)) are marked by blue, red and green dots, respectively. We note that even we mark them in the same colors as Fig. 2, only the parabolic state 2 (green) is completely distributed on layer B. In contrast, the other states are no longer confined in the corresponding layers due to the increasing layer hybridization at these small twist angles, as can be seen from the layer-projected band structure in Fig. S2 in Supplementary Materials. Figure 3(d) also shows the splitting  $\Delta$  between the parabolic states 1 and 2, and a crossing between them is found at an angle smaller than one degree. Interestingly, the eigenvalue of parabolic state 2 (green) is found to be pinned at a certain value for all twist angles in our TB calculations. This indicates that parabolic state 2 is decoupled from the others. Therefore, we set the energy of parabolic state 2 to be zero in Fig. 3(a) and (c) as reference point. The reason for the special pinning of parabolic state 2 lies in its characteristic wavefunction, which occupies only sublattice  $S_B$  in layer B [see the convention of sublattices in Fig. 2(d)]. For any given site of sublattice  $S_B$  in layer B, its effective interlayer couplings to the sites in the adjacent layer A nearly cancel out at the K point, and its interaction with the twisted monolayer is neglected in the TB model. Consequently, parabolic state 2 is completely decoupled from the others, and thus its wavefunction remains unchanged for all twist angles with a pinned eigenvalue. On the other hand, the Dirac cone shifts upwards in energy [21, 22, 26] relative to parabolic state 2. When  $\theta$  approaches  $1.3^\circ$ , the Dirac cone splits into two states. Interestingly, the twist angle at which the splitting of Dirac bands occurs coincides with that when the Dirac bands shift to the topmost position.

#### D. Layer-dependent charge localization and delocalization

Charge localization observed in the AA region of TBG plays an important role in enhancing the electron's coulomb interaction [31–33]. In this work, we study the

flat bands of aAB with layer-resolved charge distribution for a twist angle of  $\theta = 1.20^\circ$  as shown in Fig. 4(a). Similar to TBG, we find that the adjacent twisted layers (a and A layers) exhibit clear charge localization in the AAB region, consistent with the findings in several experiments [16, 34]. On the contrary, the charge distribution on the outer bilayer (layer B) demonstrates a delocalized nature. Our results indicate that charge localization and delocalization coexist in the aAB system near the qMA [34]. Approximately 40% of the charge is distributed on layer B, and 30% on each of the other layers when integrated over the four flat bands. The charge redistribution induced by an electric field will be further investigated later. Figure 4(b) illustrates the sublattice-dependent charge distribution along the high-symmetry line in real space from CAB, AAB to BAB. Our findings reveal that the charge distribution on layer B is completely sublattice polarized, with only sublattice  $S_B$  being occupied. This indicates the non-trivial band topology of aAB flat bands. Based on the similarity between charge localization in the adjacent twisted layers of aAB and TBG, as well as the near delocalization of charge in layer B, we can regard the aAB system as TBG perturbed by an additional Bernal layer when only the four low-energy bands are considered. This additional graphene layer shares the charge from TBG and further modifies the low-energy bands, but at the same time keeps some characteristics of TBG, such as the qMA at which the low-energy bands have a minimum band width.

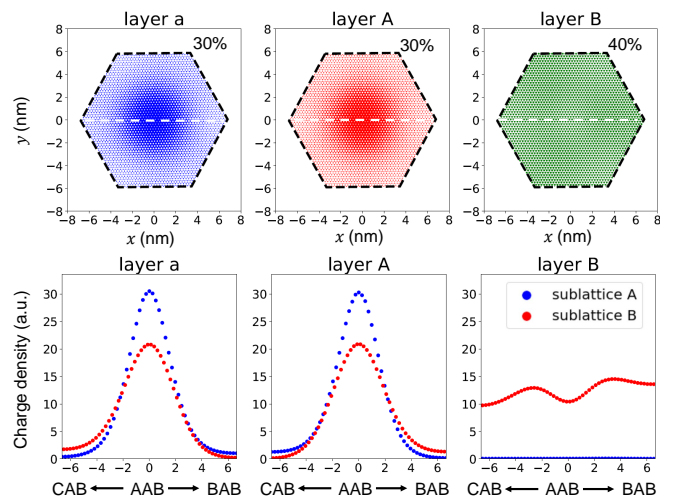


FIG. 4. (a) Layer-resolved charge distribution integrated over the four flat bands of aAB at  $\theta = 1.20^\circ$ . The charge is localized in the AAB region on layers a and A while delocalized on layer B. (b) Sublattice-resolved charge distribution along the white dashed line in (a), going through the CAB, AAB to BAB regions. The charge distribution in layer B is completely sublattice polarized.



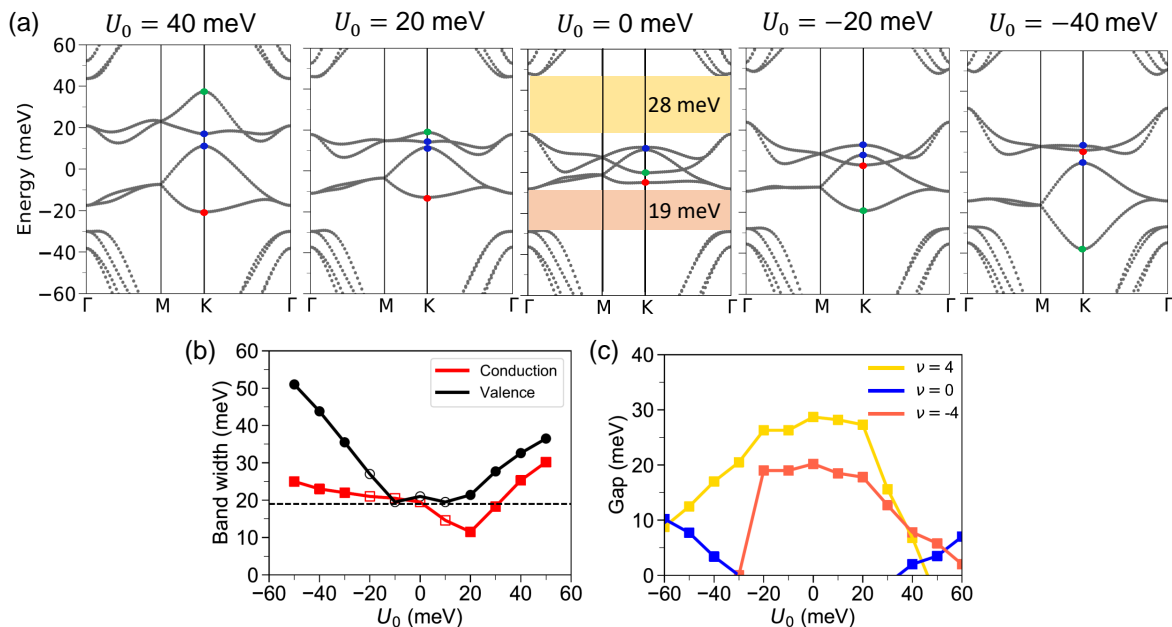


FIG. 5. (a) Band structure as a function of electrostatic potential energy  $U_0$  at a twist angle  $\theta = 1.20^\circ$ . In these figures, lattice relaxation of aAB is considered. The yellow and pink regions mark the gaps at full and empty fillings in the absence of an electric field ( $U_0 = 0$ ), which is attributed to the lattice relaxation effect. The zero energy is set at the pinned eigenvalue of parabolic state 2 (green) when  $U_0 = 0$ . The blue, red, and green dots are the Dirac states, parabolic states 1 and 2, respectively. (b) Band width of the conduction bands and the valence bands under the electric field. Hollow points indicate that the bands overlap near the K point. (c) Band gaps at  $\nu = 0, 4$  and  $-4$  for different electric fields.

### E. Lattice relaxation effect on the low-energy bands

Structural relaxation plays an important role in opening gaps at full and empty fillings of the flat bands in TBG. In this work, we find that lattice relaxation in aAB also has a significant impact on the low-energy bands. The lattice relaxation pattern is calculated based on an  $O(n)$  method implemented in OpenMX [35, 36], and the detail of our result is presented in Supplementary Materials. The band structure of aAB when lattice relaxation is taken into account at  $\theta = 1.20^\circ$  is shown in the middle of Fig. 5 (in the absence of electric field  $U_0 = 0$ ). It can be seen that large band gaps of about 30 and 20 meV develop at full and empty fillings, marked by yellow and pink regions. The formation of gaps separate the four flat bands from other remote bands. In the next section, we will discuss the structural relaxation effect on the low-energy bands when an external electric field is applied to aAB.

### F. Electrically tunable flat bands and bands gaps

It was observed in experiments that an out-of-plane electric field leads to the emergence of an energy gap at the charge neutrality point (CNP) for aAB [14, 15, 17]. To study the electric field effect on the low-energy bands near the qMA, we applied potential energies  $-U_0, 0$ , and

$U_0$  to layers a, A, and B, respectively, in our TB model. For  $U_0 > 0$ , the displacement field points from the monolayer to the bilayer graphene. Figure 5(a) shows the aAB band structures at  $\theta = 1.20^\circ$  with different values of  $U_0$ , and lattice relaxation is taken into account in these calculations. The blue, red and green dots in these band structures represent the Dirac states, parabolic states 1 and 2 as defined previously. In Fig. 5(a), the energy zero is set at the pinned eigenvalue of the parabolic state 2 (green) in the absence of electric field ( $U_0=0$ ). In this way, we can directly compare the energy variation of each state for different values of  $U_0$ . The energy variations of the parabolic states 1 and 2 under the electric field differ due to the difference in charge distribution on the layers, therefore allowing tunable splitting between them, as was observed in a recent ARPES measurement [37].

Importantly, the splitting of the Dirac states (blue) can also be tuned by the electric field, and an energy gap at the CNP gradually opens for both directions of the electric field. This electric-field induced energy gap thus separates the conduction flat bands from the valence flat bands. In contrast, when lattice relaxation is not considered in the calculations, the electric field cannot tune the splitting of the Dirac cone, and the energy gap at the CNP does not open (see Fig. S3 in Supplementary Materials). Therefore, we demonstrate that the structural relaxation effect is a crucial factor when studying the electrically tunable flat bands and band gaps in aAB.

Figure 5(b) shows the band width of the conduction

bands and valence bands under various applied electric fields. The solid data points represent the band widths of the well-separated conduction and valence bands are well separated, while the hollow points indicate that they overlap near the K point. In general, the band width of the conduction bands is smaller than the valence bands in the presence of an electric field. In particular, when the electrostatic potential energy is about 20 meV, the conduction flat bands has a minimum band width of roughly 10 meV. The formation of conduction flat bands at a positive  $U_0$  explains the emergence of correlated insulating phases on the electron doping side when an electric field is applied from the monolayer to the bilayer in the experiments [14–18, 20]. In addition, the band gaps at  $\nu = 0, 4$  and  $-4$  (corresponding to CNP, full and empty fillings, respectively) can also be tuned by the electric field as shown in Fig. 5(c). In our calculations, the band gap at  $\nu = 0$  opens when the electrostatic potential energy is about 30 meV for both directions, and the single-particle gaps at  $\nu = 4$  and  $-4$  disappear in some circumstances when the electric field is strong enough. From our band structure calculations, the diversity of electrically tunable flat bands and gaps can be attributed to two intrinsic factors in aAB: (1) The presence of strong particle-hole asymmetry leads to different electronic properties for the conduction and valence bands, and (2) the low crystal symmetry results in distinct electrical responses for the two orientations of the electronic field.

### G. Charge transfer and redistribution under the electric field

In the aAB system, we have demonstrated the layer-dependent charge localization and delocalization patterns near the qMA. When an electric field is applied, charge transfer and redistribution are expected to happen. A particularly interesting feature is the charge distribution of the conduction flat bands and the valence flat bands when the electric-field-induced gap separates them. Since these flat bands carry different Chern numbers [21–23], their spatial charge distributions are also expected to be distinct and unique.

Here, we demonstrate the layer-resolved charge distribution for the conduction flat bands at  $U_0 = 20$  meV as shown in Fig. 6. We observe that a large portion (nearly 60%) of charge is contributed from layer B, and it features a delocalized distribution. Similar to the case when the electric field is absent, the charge in layer B is still sublattice polarized. In contrast, the charge in layers a and A is localized only on sublattice A, and delocalized on sublattice B. On the other hand, for the valence bands at  $U_0 = 20$  meV, only 29% of the charge distributes in layer B as shown in Fig. S7. On layers a and A, the sublattice-dependent localization and delocalization patterns are still present, but with a reversal of sublattice compared with the conduction bands. Our discovery unravels that both the conduction and valence bands feature the coex-

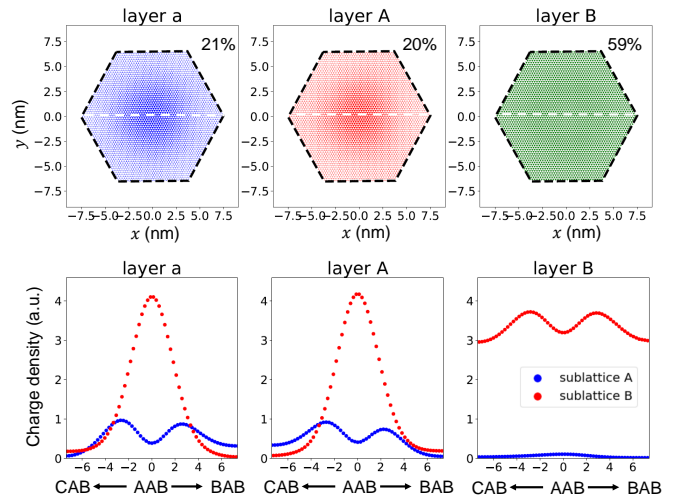


FIG. 6. Layer-resolved charge distribution for the conduction flat bands of aAB at  $U_0 = 20$  meV. Charge transfer acrosses layers and leads to a greater amount of charge in layer B (nearly 60%). Meanwhile, although the charge on layers a and A is still localized in the AAB region, the spatial localization only occurs at one sublattice  $S_A$ . The lower panels show the special sublattice-dependent charge localization and delocalization patterns. Interestingly, the charge distributions at sublattice  $S_A$  in layers a and A have a similar delocalization pattern as sublattice  $S_B$  in layer B.

istence of a unique sublattice-dependent charge localization and delocalization within a single graphene layer.

When the electric field is swept to the opposite direction, a reversed charge transfer and redistribution is observed. For example, the charge distribution for the conduction bands at  $U_0 = -40$  meV (Fig. S8) is similar to that for the valence bands at  $U_0 = 20$  meV (Fig. S7). The reversal of charge distribution in the valence and conduction bands when the electric field is applied in the opposite direction is an indication of the Chern number switching between these flat bands. Since the Chern numbers of these flat bands in previous studies vary from each other due to different parameters in the models [21–23], the unique and distinct charge distribution we observed using an accurate tight-binding model can serve as a reference for the quantum textures of these flat bands for future theoretical investigations.

## III. CONCLUSION

In this work, we have used first-principles calculations combined with an accurate tight-binding model to study the electronic properties of the aAB system. Our calculations uncover the existence of an intrinsic polarization due to an asymmetric charge transfer across layers, resulting in a significant splitting of the parabolic bands at a large twist angle, highlighting the importance of an accurate model calculation. We further define the quasi-magical angle of aAB at  $\theta = 1.16^\circ$ , at which aAB has a

minimum width of the four flat bands. Near the quasi-magic angle, the four flat bands feature charge localization in layers a and A, and a delocalization pattern in layer B, consistent with prior experimental observations. In the presence of an out-of-plane electric field, we discover that the CNP gap only opens when lattice relaxation is taken into account, indicating the importance of structural relaxation effects. Moreover, the electric field can further tune the band gaps as well as the width of the flat bands, with the conduction bands generally being flatter than the valence bands. This explains why the correlated states were observed only on the electron doping side. For both the conduction and valence bands, the charge distributions in a and A layers are only localized at one sublattice. This unique sublattice-dependent localization and delocalization can further be reversed by the orientations of an external electric field. With an atomic-scale STM measurement, one would be able to observe this special layer and sublattice-dependent charge distribution. The quantum texture of these flat bands demonstrated in our work would serve as a starting point for exploring the electron correlation in the aAB system.

#### IV. METHOD

##### A. Density functional theory calculations

In this work, we perform density functional theory (DFT) calculations to study the electronic structure of aAB at large twist angles. We use the Vienna Ab initio Simulation Package (VASP) [38, 39] with the projector-augmented wave method [40, 41] and the exchange-

correlation functional GGA [42]. The plane-wave cut-off energy is 500 eV. We use a  $\Gamma$ -centered k-point mesh of  $12 \times 12 \times 1$ ,  $9 \times 9 \times 1$ ,  $6 \times 6 \times 1$  and  $3 \times 3 \times 1$  for aAB supercells with  $\theta = 13.2^\circ$  ( $m=2$ ),  $\theta = 9.4^\circ$  ( $m=3$ ),  $\theta = 5.1^\circ$  ( $m=6$ ), and  $\theta = 3.1^\circ$  ( $m=10$ ). In addition, the Berry phase method [27] is used to calculate the dipole moment of the supercells with a denser k-point mesh:  $18 \times 18 \times 1$  for  $\theta = 13.2^\circ$  ( $m=2$ ). A vacuum of 15 Å is used in our calculations in order to prevent interactions between artificial periodic images. On the other hand, lattice relaxations of the moiré supercells are calculated by an O(n) method implemented in OpenMX [35, 36]. We use the divide-and-conquer scheme with localized natural orbitals (DCLNO) [43]. A local density approximation (LDA) is used for the exchange-correlation functional with a cut-off energy of 250 Ry. The structure is relaxed until the force on each atom is less than 0.01 eV/Å.

##### B. Tight-binding calculations

An accurate tight-binding (TB) model with angle-dependent parameters [24, 25] is used to investigate the electronic properties of aAB. In our TB calculations, we take into account eight nearest-neighbor intralayer couplings. For interlayer couplings, we include the hoppings when the projected in-plane distance between two atoms is smaller than the fifth nearest neighbor distance. The integrated charge distribution for the four flat bands was calculated using a  $\Gamma$ -centered k-point mesh of  $18 \times 18 \times 1$ . For unrelaxed systems, the interlayer distances between adjacent layers are set as  $d = 3.35$  Å.

- 
- [1] Y. Cao, V. Fatemi, A. Demir, S. Fang, S. L. Tomarken, J. Y. Luo, J. D. Sanchez-Yamagishi, K. Watanabe, T. Taniguchi, E. Kaxiras, R. C. Ashoori, and P. Jarillo-Herrero, Correlated insulator behaviour at half-filling in magic-angle graphene superlattices, *Nature* **556**, 80–84 (2018).
  - [2] X. Lu, P. Stepanov, W. Yang, M. Xie, M. A. Aamir, I. Das, C. Urgell, K. Watanabe, T. Taniguchi, G. Zhang, A. Bachtold, A. H. MacDonald, and D. K. Efetov, Superconductors, orbital magnets and correlated states in magic-angle bilayer graphene, *Nature* **574**, 653–657 (2019).
  - [3] Y. Cao, V. Fatemi, S. Fang, K. Watanabe, T. Taniguchi, E. Kaxiras, and P. Jarillo-Herrero, Unconventional superconductivity in magic-angle graphene superlattices, *Nature* **556**, 43–50 (2018).
  - [4] A. L. Sharpe, E. J. Fox, A. W. Barnard, J. Finney, K. Watanabe, T. Taniguchi, M. A. Kastner, and D. Goldhaber-Gordon, Emergent ferromagnetism near three-quarters filling in twisted bilayer graphene, *Science* **365**, 605 (2019).
  - [5] K. P. Nuckolls, M. Oh, D. Wong, B. Lian, K. Watanabe, T. Taniguchi, B. A. Bernevig, and A. Yazdani, Strongly correlated chern insulators in magic-angle twisted bilayer graphene, *Nature* **588**, 610–615 (2020).
  - [6] S. Wu, Z. Zhang, K. Watanabe, T. Taniguchi, and E. Y. Andrei, Chern insulators, van hove singularities and topological flat bands in magic-angle twisted bilayer graphene, *Nature Materials* **20**, 488–494 (2021).
  - [7] Y. Xie, A. T. Pierce, J. M. Park, D. E. Parker, E. Khalaf, P. Ledwith, Y. Cao, S. H. Lee, S. Chen, P. R. Forrester, *et al.*, Fractional chern insulators in magic-angle twisted bilayer graphene, *Nature* **600**, 439–443 (2021).
  - [8] J. M. Park, Y. Cao, K. Watanabe, T. Taniguchi, and P. Jarillo-Herrero, Tunable strongly coupled superconductivity in magic-angle twisted trilayer graphene, *Nature* **590**, 249 (2021).
  - [9] Z. Hao, A. M. Zimmerman, P. Ledwith, E. Khalaf, D. H. Najafabadi, K. Watanabe, T. Taniguchi, A. Vishwanath, and P. Kim, Electric field-tunable superconductivity in alternating-twist magic-angle trilayer graphene, *Science* **371**, 1133 (2021).
  - [10] X. Liu, N. J. Zhang, K. Watanabe, T. Taniguchi, and J. I. Li, Isospin order in superconducting magic-angle twisted trilayer graphene, *Nature Physics* **18**, 522–527 (2022).

- [11] Y. Xie, B. Lian, B. Jäck, X. Liu, C. L. Chiu, K. Watanabe, T. Taniguchi, B. A. Bernevig, and A. Yazdani, Spectroscopic signatures of many-body correlations in magic-angle twisted bilayer graphene, *Nature* **572**, 101–105 (2019).
- [12] E. Khalaf, A. J. Kruchkov, G. Tarnopolsky, and A. Vishwanath, Magic angle hierarchy in twisted graphene multilayers, *Physical Review B* **100**, 085109 (2019).
- [13] S. Carr, C. Li, Z. Zhu, E. Kaxiras, S. Sachdev, and A. Kruchkov, Ultraheavy and ultrarelativistic Dirac quasiparticles in sandwiched graphenes, *Nano Letters* **20**, 3030 (2020).
- [14] S. Chen, M. He, Y. H. Zhang, V. Hsieh, Z. Fei, K. Watanabe, T. Taniguchi, D. H. Cobden, X. Xu, C. R. Dean, and M. Yankowitz, Electrically tunable correlated and topological states in twisted monolayer–bilayer graphene, *Nature Physics* **17**, 374–380 (2021).
- [15] S. Xu, M. M. A. Ezzi, N. Balakrishnan, A. Garcia-Ruiz, B. Tsim, C. Mullan, J. Barrier, N. Xin, B. A. Piot, T. Taniguchi, K. Watanabe, A. Carvalho, A. Mishchenko, A. K. Geim, V. I. Fal’ko, S. Adam, A. H. C. Neto, K. S. Novoselov, and Y. Shi, Tunable van Hove singularities and correlated states in twisted monolayer–bilayer graphene, *Nature Physics* **17**, 619–626 (2021).
- [16] S. Yu Li, Z. Wang, Y. Xue, Y. Wang, S. Zhang, J. Liu, Z. Zhu, K. Watanabe, T. Taniguchi, H. Jun Gao, Y. Jiang, and J. Mao, Imaging topological and correlated insulating states in twisted monolayer–bilayer graphene, *Nature Communications* **13**, 4225 (2022).
- [17] H. Polshyn, J. Zhu, M. A. Kumar, Y. Zhang, F. Yang, C. L. Tschirhart, M. Serlin, K. Watanabe, T. Taniguchi, A. H. MacDonald, and A. F. Young, Electrical switching of magnetic order in an orbital Chern insulator, *Nature* **588**, 66–70 (2020).
- [18] C. Zhang, T. Zhu, T. Soejima, S. Kahn, K. Watanabe, T. Taniguchi, A. Zettl, F. Wang, M. P. Zaletel, and M. F. Crommie, Local spectroscopy of a gate-switchable moiré quantum anomalous Hall insulator, *Nature Communications* **14**, 3595 (2023).
- [19] H. Polshyn, Y. Zhang, M. A. Kumar, T. Soejima, P. Ledwith, K. Watanabe, T. Taniguchi, A. Vishwanath, M. P. Zaletel, and A. F. Young, Topological charge density waves at half-integer filling of a moiré superlattice, *Nature Physics* **18**, 42–47 (2022).
- [20] M. He, Y. H. Zhang, Y. Li, Z. Fei, K. Watanabe, T. Taniguchi, X. Xu, and M. Yankowitz, Competing correlated states and abundant orbital magnetism in twisted monolayer–bilayer graphene, *Nature Communications* **12**, 4727 (2021).
- [21] Y. Park, B. L. Chittari, and J. Jung, Gate-tunable topological flat bands in twisted monolayer–bilayer graphene, *Physical Review B* **102**, 035411 (2020).
- [22] Z. Ma, S. Li, Y. W. Zheng, M. M. Xiao, H. Jiang, J. H. Gao, and X. C. Xie, Topological flat bands in twisted trilayer graphene, *Science Bulletin* **66**, 18 (2021).
- [23] L. Rademaker, I. V. Protopopov, and D. A. Abanin, Topological flat bands and correlated states in twisted monolayer–bilayer graphene, *Physical Review Research* **2**, 033150 (2020).
- [24] S. Fang and E. Kaxiras, Electronic structure theory of weakly interacting bilayers, *Physical Review B* **93**, 235153 (2016).
- [25] S. Carr, S. Fang, P. Jarillo-Herrero, and E. Kaxiras, Pressure dependence of the magic twist angle in graphene superlattices, *Physical Review B* **98**, 085144 (2018).
- [26] E. S. Morell, M. Pacheco, L. Chico, and L. Brey, Electronic properties of twisted trilayer graphene, *Physical Review B - Condensed Matter and Materials Physics* **87**, 125414 (2013).
- [27] R. D. King-Smith and D. Vanderbilt, Theory of polarization of crystalline solids, *Physical Review B* **47**, 1651 (1993).
- [28] P. Rickhaus, G. Zheng, J. L. Lado, Y. Lee, A. Kurzman, M. Eich, R. Pisoni, C. Tong, R. Garreis, C. Gold, M. Masseroni, T. Taniguchi, K. Watanabe, T. Ihn, and K. Ensslin, Gap opening in twisted double bilayer graphene by crystal fields, *Nano Letters* **19**, 8821–8828 (2019).
- [29] F. J. Culchac, R. R. D. Grande, R. B. Capaz, L. Chico, and E. S. Morell, Flat bands and gaps in twisted double bilayer graphene, *Nanoscale* **12**, 5014 (2020).
- [30] F. Haddadi, Q. S. Wu, A. J. Kruchkov, and O. V. Yazyev, Moiré flat bands in twisted double bilayer graphene, *Nano Letters* **20**, 2410–2415 (2020).
- [31] G. Li, A. Luican, J. M. L. D. Santos, A. H. C. Neto, A. Reina, J. Kong, and E. Y. Andrei, Observation of van Hove singularities in twisted graphene layers, *Nature Physics* **6**, 109–113 (2010).
- [32] I. Brihuega, P. Mallet, H. González-Herrero, G. T. D. Laissardière, M. M. Ugeda, L. Magaud, J. M. Gómez-Rodríguez, F. Ynduráin, and J. Y. Veuillen, Unraveling the intrinsic and robust nature of van Hove singularities in twisted bilayer graphene by scanning tunneling microscopy and theoretical analysis, *Physical Review Letters* **109**, 196802 (2012).
- [33] A. Kerelsky, L. J. McGilly, D. M. Kennes, L. Xian, M. Yankowitz, S. Chen, K. Watanabe, T. Taniguchi, J. Hone, C. Dean, A. Rubio, and A. N. Pasupathy, Maximized electron interactions at the magic angle in twisted bilayer graphene, *Nature* **572**, 95–100 (2019).
- [34] L. H. Tong, Q. Tong, L. Z. Yang, Y. Y. Zhou, Q. Wu, Y. Tian, L. Zhang, L. Zhang, Z. Qin, and L. J. Yin, Spectroscopic visualization of flat bands in magic-angle twisted monolayer–bilayer graphene: Coexistence of localization and delocalization, *Physical Review Letters* **128**, 126401 (2022).
- [35] T. Ozaki, Variationally optimized atomic orbitals for large-scale electronic structures, *Physical Review B - Condensed Matter and Materials Physics* **67**, 155108 (2003).
- [36] T. Ozaki and H. Kino, Efficient projector expansion for the ab initio LCAO method, *Physical Review B - Condensed Matter and Materials Physics* **72**, 045121 (2005).
- [37] J. E. Nunn, A. McEllistrim, A. Weston, A. Garcia-Ruiz, M. D. Watson, M. Mucha-Kruczynski, C. Cacho, R. V. Gorbachev, V. I. Fal’ko, and N. R. Wilson, Arpes signatures of few-layer twistrionic graphenes, *Nano Letters* , 5201–5208 (2023).
- [38] G. Kresse and J. Furthmüller, Efficient iterative schemes for ab initio total-energy calculations using a plane-wave basis set, *Physical Review B - Condensed Matter and Materials Physics* **54**, 11169 (1996).
- [39] G. Kresse and J. Furthmüller, Efficiency of ab-initio total energy calculations for metals and semiconductors using a plane-wave basis set, *Computational Materials Science* **6**, 15 (1996).
- [40] P. E. Blöchl, Projector augmented-wave method, *Physical Review B* **50**, 17953 (1994).



- [41] D. Joubert, From ultrasoft pseudopotentials to the projector augmented-wave method, [Physical Review B - Condensed Matter and Materials Physics](#) **59**, 1758 (1999).
- [42] J. P. Perdew, K. Burke, and M. Ernzerhof, Generalized gradient approximation made simple, [Physical Review Letters](#) **77**, 3865 (1996).
- [43] T. Ozaki, M. Fukuda, and G. Jiang, Efficient  $\mathcal{O}(n)$  divide-conquer method with localized single-particle natural orbitals, [Physical Review B](#) **98**, 245137 (2018).